

Journal of Materials Chemistry A

Accepted Manuscript



This is an *Accepted Manuscript*, which has been through the Royal Society of Chemistry peer review process and has been accepted for publication.

Accepted Manuscripts are published online shortly after acceptance, before technical editing, formatting and proof reading. Using this free service, authors can make their results available to the community, in citable form, before we publish the edited article. We will replace this *Accepted Manuscript* with the edited and formatted *Advance Article* as soon as it is available.

You can find more information about *Accepted Manuscripts* in the [Information for Authors](#).

Please note that technical editing may introduce minor changes to the text and/or graphics, which may alter content. The journal's standard [Terms & Conditions](#) and the [Ethical guidelines](#) still apply. In no event shall the Royal Society of Chemistry be held responsible for any errors or omissions in this *Accepted Manuscript* or any consequences arising from the use of any information it contains.

**Simultaneously Covalent and Ionic Bridging towards Antifouling of GO-embedded
Nanocomposite Hollow Fiber Membranes**

Yu Pan Tang^a, Jing Xiong Chan^a, Tai Shung Chung^{a,*},
Martin Weber^b, Claudia Staudt^c, Christian Maletzko^d

^a Department of Chemical and Biomolecular Engineering, National University of Singapore,
4 Engineering Drive 4, Singapore 117585

^b Advanced Materials & Systems Research BASF SE, GMV/W - B001, 67056 Ludwigshafen,
Germany

^c Advanced Materials & Systems Research, BASF SE, GMM/M-B001, 67056 Ludwigshafen,
Germany

^d Performance Materials, BASF SE, G-PM/PU, 67056 Ludwigshafen, Germany

*Corresponding author

Email: chencts@nus.edu.sg

Fax : (65)-67791936

Abstract

A group of GO-imbedded nanocomposite hollow fiber membranes was investigated for oily water treatment, with the objectives of improving GO-polymer interfacial interaction and membrane anti-fouling properties via the formation of a simultaneously covalent and ionic inter-network. 1-Methylnicotinamide chloride (MNA) was selected to bridge the two parties. The reaction scheme was proposed and evidenced by FTIR and XRD analyses. The resultant membranes were systematically studied with respect to membrane microstructure, ultrafiltration performance and fouling behaviors. The responses of the membranes to oil-water fouling were evaluated by the resistance-in-series model and cyclic UF experiments with periodic backwashing. It appears that the membrane with a GO:MNA ratio of 9:1 was found to exhibit the most favorable properties for oil-water separation. Substantial reductions in reversible, irreversible and adsorption-induced resistances as well as flux drop were observed. Generally, the superior anti-fouling properties of the nanocomposite membrane benefit from the contributions of (1) the hydrophilic nature of GO and MNA, (2) appropriate GO:MNA ratio and (3) synergetic effects between GO and MNA to overcome the interfacial voids and produce a balanced membrane structure. In addition to unveiling the importance of interfacial interaction between GO nanofillers and polymer matrices, this work may pave the way to design advanced GO-imbedded anti-fouling nanocomposite membranes for the years to come.

Key words: Graphene oxide, Interfacial interaction, anti-fouling, ultrafiltration, oil-water separation

1. Introduction

Membrane filtration is regarded as an energy-efficient and cost-effective approach for oily wastewater treatment ¹⁻³ in comparison to the conventional methods ³, e.g. floatation, adsorption and flocculation. On account of the increasingly generated oil-water emulsion in diverse industries ^{4, 5}, the development of anti-fouling membranes is one of the most important imperatives in order to meet the discharging requirements of oily wastewater ⁶. Currently, membrane fouling is still an inevitable challenge in various membrane applications. Generally, membrane fouling is caused by complicated interactions between solutes and membranes pertaining to their physicochemical and biological properties, which result in degradation of separation capabilities and membrane properties ⁷⁻⁹. Thus, in addition to the optimization of operating conditions, molecular design of the membrane materials with balanced physicochemical properties would be an alternative approach to eliminate fouling.

Extensive research ¹⁰⁻¹⁴ has shown that by increasing membrane hydrophilicity, water molecules would be attracted towards the membrane surface to form a hydration layer, thereby interfering with the adhesion of foulant molecules to the membrane surface. This mechanism inhibits the deposition of solute particles onto the membrane surface or within the membrane pores and hence improves the anti-fouling properties of a membrane. An facile approach to implement this mechanism is to fabricate organic-inorganic composite membranes via incorporation of hydrophilic inorganic nanoparticles, e.g., TiO₂ ¹⁵⁻¹⁷, Al₂O₃ ¹⁸, graphene oxide (GO) ¹⁹⁻²¹ into the polymer matrix. Amongst various hydrophilic materials, graphene oxide (GO) has received increasing attention in recent years due to its exceptionally chemical, physical and mechanical properties ²²⁻²⁴. The abundant oxygen-containing groups on the graphene nanosheet enable it to be stably dispersed in a variety of solvents, e.g. water, n-methyl-2-pyrrolidone (NMP) and dimethylformamide (DMF), and chemically modified.

Recently, attempts have been made to explore the functions of GO in different polymeric matrices with respect to their anti-fouling properties in UF processes. Wang et al¹⁹ and Zhao et al²⁵ found a noticeable increment in flux recovery ratio (FRR) by blending GO nanosheets in polyvinylidene fluoride (PVDF), which signified the improved anti-fouling properties. Similar results were observed in polyethersulfone (PES)-GO²⁰ and polysulfone (PS)-GO²⁶ composite membranes. In addition to the bare GO, functionalized GO nanoparticles as membrane fillers were also reported²⁷⁻³⁰. For example, Yang et al²⁷ and Yu et al²⁸ introduced branched polyethylenimine-modified GO particles in PES membranes. They found a remarkable reduction in contact angle but a slightly increase in FRR probably due to the rougher membrane surface created by the fillers. Similarly, organosilane²⁹ and isocyanate³⁰ were used to treat GO particles in order to be well-dispersed in organic solvents. An increase in FRR during protein separation was observed owing to the increased hydrophilicity, higher negative zeta potential and lower surface roughness brought by the GO modifications. Additionally, synergistic effects between GO and other inorganic particles were also investigated³¹⁻³⁴. For example, Zhang et al^{33,34} found that the agglomeration of GO could be effectively mitigated by the long and tortuous oxidized carbon nanotubes (OMWCNTs) in a flat-sheet PVDF membrane because OMWCNTs can bridge adjacent GO and improve the fillers' dispersibility. As a result, the GO-OMWCNTs-modified membrane showed a high wettability to prevent cake formation on membrane surface.

Although GO-incorporated composite membranes for ultrafiltration applications have unveiled remarkable improvements in anti-fouling properties, some of their drawbacks need to be carefully addressed. The major one is the poor dispersion of GO particles within the polymer matrix owing to weak interfacial interactions between the two components³⁵.

Except for limited cases, most of work failed to provide useful insights about the interfacial interactions between GO nanosheets and polymer matrices. Additionally, surface roughness is another important factor to fouling formation as foulants would be physically trapped in the valleys of a rough surface. Some work in literatures have demonstrated that surface roughness appears to increase after incorporating GO particles, which would weaken the anti-fouling properties^{27, 29, 32}. Thus, the optimal conditions to fabricate high-performance GO-embedded nanocomposite membrane need to be carefully examined. In this work, we attempt to improve the performance of GO-embedded nanocomposite hollow fiber membranes by introducing 1-methylnicotiamide chloride (MNA) which serves as the bridge to improve the interfacial interactions between the GO nanosheets and the sPPSU polymer. The reaction scheme involves both covalent and ionic interlink, which was evidenced via Fourier transform infrared spectroscopy (FTIR) and X-ray photoelectron spectroscopy (XPS) analyses. The changes in microstructure of the nanocomposite membranes were studied by field emission scanning electron microscopy (FESEM) and atomic force microscopy (AFM), etc. Additionally, an analysis of fouling mechanism and cyclic UF experiments with periodic backwashing were performed to investigate the membrane response to fouling for oil-water separation.

2. Experimental

2.1. Materials

The sulfonated polyphenylenesulfone (sPPSU) was synthesized via the directly copolymerized sulfonation method³⁶ with 1.5 mol% 3,3'-disulfonate-4,4'-dichlorodiphenyl sulfone (sDCDPS) monomer in the copolymerization reaction. Figure S1 shows the molecular structure of the sPPSU polymer. N-methyl-2-pyrrolidone (NMP, AR) and polyethylene glycol 400 (PEG400, AR) were purchased from Merck and used as the solvent

and pore former, respectively. Polyethylene oxide (PEO) polymers with different molecular weights of 20, 35, 100 and 200 KDa were used to characterize the molecular weight cut-off (MWCO) and pore size of the membranes. An aqueous GO solution (0.5 wt%) was purchased from Angstrom Materials Inc. The GO nanosheets are about 1 nm thick with a lateral length less than 1 μm as characterized in a previous publication³⁷. 1-Methylnicotinamide chloride (MNA, $\geq 98\%$ HPLC) was purchased from Sigma-Aldrich. For the oil-water emulsion, a petroleum with an aromatics basis of about 18% was used as the oil component and Lutensol[®] XL 80 provided by BASF SE as the surfactant.

2.2. Dope preparation and hollow fiber spinning

The 0.5 wt% GO solution was firstly concentrated via vacuum distillation in a Heidolph Instruments Laborota 4010 rotary evaporator until a sludgy solution was attained. Afterwards, a certain amount of NMP was added, followed by 2-h of sonication to form a stable GO suspension in the mixed solvent. The resultant solution had a composition of 0.35/25.48/74.17 wt% of GO/H₂O/NMP.

The MNA-modified GO (MGO)-incorporated dope solutions were prepared following the procedures indicated in Figure S2. Generally, a certain amount of MNA was firstly dissolved in NMP. A small portion of the sPPSU polymer was then added to form a dilute polymer solution in order to prevent MNA and GO nanosheets from agglomeration. Once the GO nanosheets were uniformly dispersed in the dilute polymer solution, the rest of the sPPSU polymer was added. After being fully dissolved, the MNA/GO/sPPSU solution was heated to 80 °C in an oven for 1 h to promote the reaction between MNA and GO nanosheets³⁸. For comparison, GO-sPPSU and sPPSU dope solutions were also prepared following the similar procedures.

The dope solutions were loaded in the spinning system after being fully degassed. The detailed description of single-layer hollow fiber spinning can be found in previous publications^{39, 40}. Except for those listed in Table 1 and Table 2, all other spinning parameters were kept constant: A single-layer spinneret with an outer diameter of 2.0 mm, tap water as the external coagulant and ambient temperature (23 ± 2 °C) for spinning. In addition, the air gap length was kept at 20 mm, the dope flow rate at 10 mL/min and the take up speed at 11-12 m/min in a free-fall manner. As for the spinning of GO- and MGO-incorporated nanocomposite hollow fiber membranes in Table 2, the total solid content is 12 wt% where the GO concentration was kept at 0.57 wt%. Four different GO:MNA ratios, i.e., 9:1, 4:1, 2:1 and 0:1, were used to study the effects of MNA on the microstructure and fouling behaviors of the nanocomposite membranes.

Table 1

Table 2

The as-spun hollow fibers were immersed in tap water for 2 days to remove excess solvents and PEG400 within the membranes. Afterwards, two post-treatment protocols were adopted. One was to treat the membranes in a 50 wt% aqueous glycerol solution for 2 days, and then air-dried at ambient temperature. This post treatment allows the glycerol molecules to diffuse into membrane pores and prevents pore collapse during air-drying and storage. The other method was to directly dry the hollow fibers using a freeze dryer for characterization purpose.

2.3. Membrane evaluation

The physical structure of a membrane is normally evaluated by its pure water permeability (PWP) and molecular weight cut-off (MWCO). MWCO is a loosely defined term generally measuring the molecular weight of globular solute molecules in which 90% of the solute is

retained by the membrane. Instead of globular molecules, linear PEO molecules were used in this work. A laboratory-scale cross-flow UF system described elsewhere^{39,41} was employed to carry out all the experiments with a feed flow rate of 0.30 L/min at a transmembrane pressure (TMP) of 0.6 bar and a temperature of 23±2 °C. It should be noted that, prior to tests, all the membranes samples were washed with DI water on the UF system for 1 h at the same experimental conditions, in order to wash out the glycerol and stabilize the membrane. The mass of permeate was measured by an electronic balance (EK-4100i, A&D Company, Ltd., Japan) and recorded by a Labview program (National Instruments, Austin, TX) as a function of time. The pure water permeate flux, J_w , was calculated via the following equation:

$$J_w = \frac{M}{\rho A \Delta t} \quad (1)$$

where M is the permeate mass collected at the time interval Δt , A is the total surface area of the hollow fibers in a module and ρ is the permeate density. The PWP was calculated by:

$$PWP = \frac{J_w}{TMP} \quad (2)$$

To evaluate the MWCO and pore size, PEO solutions with a concentration of 200 ppm were used. The feed solution and permeate samples were collected at an interval of 30 min after conditioning for 1 h. The PEO content of the samples were then analyzed using a total organic carbon (TOC) Analyzer. The rejection R was calculated by the following equation:

$$R (\%) = \left(1 - \frac{C_p}{C_f}\right) \times 100\% \quad (3)$$

where C_p and C_f are the concentrations of permeate and feed, respectively.

2.4. Fouling evaluation

Fouling behaviors of the nanocomposite membranes were evaluated using an oil-water emulsion. The method to prepare the oil-water emulsion was introduced elsewhere⁴². Generally, 1.0 g Lutensol® XL 80 surfactant and 9.0 g petroleum oil were added to 990.0 g

DI water, and the mixture was then blended in a stainless steel blender (Waring 7011S) for 3 min. The emulsion containing 10,000 ppm oil was further diluted to 2,000 ppm.

The antifouling properties of the membranes were evaluated via the resistance-in-series model⁴³ and cyclic UF experiments with periodic backwashing. Mathematically, the resistance-in-series model is represented by the following equation:

$$R_t = R_m + R_{ads} + R_r + R_{ir} \quad (4)$$

Where R_t is the total membrane resistance, while R_m , R_{ads} , R_r and R_{ir} refer to the resistances induced by the membrane itself, adsorption, reversible fouling and irreversible fouling, respectively.

Membrane hydraulic resistance, R_m

The value of R_m was determined by the following equation:

$$R_m = \frac{1}{\mu PWP} \quad (5)$$

Where μ is the viscosity of permeate.

Adsorption-induced resistance, R_{ads}

To measure R_{ads} , the membrane was firstly immersed in the oil-water emulsion for 30 min to allow oil adsorption onto the membrane surface. No external pressure was applied. Afterwards, the membrane was rinsed with DI water for 1 min to wash off the excess residual emulsion in the module and to remove loosely attached oil droplets on the membrane surface. The membrane was then tested with DI water to evaluate flux change after foulant adsorption. The total resistance was contributed by R_m and R_{ads} in this case. Hence,

$$J_{ads} = \frac{TMP}{\mu(R_m + R_{ads})} \quad (6)$$

Irreversible/reversible fouling-induced resistances, R_{ir}/R_r

To measure R_{ir} , the membrane was firstly tested using the oil-water emulsion for 1 h. The total resistance in this case was resultant from R_m , R_{ads} , R_r and R_{ir} , as represented in equation (7).

$$J = \frac{TMP}{\mu R_t} = \frac{TMP}{\mu(R_m + R_{ads} + R_r + R_{ir})} \quad (7)$$

After 1 h, backwashing with DI water was performed on the membrane for 10 min to remove oil particles that have reversibly fouled the membrane. Afterwards, the cleaned membrane was re-tested using DI water and the resistance would be attributed to only R_m and R_{ir} .

$$J_{ir} = \frac{TMP}{\mu(R_m + R_{ir})} \quad (8)$$

2.5. Characterizations

The reaction between GO and MNA were analyzed by Fourier transform infrared spectroscopy (FTIR, Bio-Rad FTS-3500) and X-ray photoelectron spectroscopy (XPS, Kratos AXIS UltraDLD, Kratos Analytical Ltd., England). In order to attain distinct FTIR results, two kinds of membranes were prepared. One is the flat-sheet membrane cast via the phase inversion method using the same dope solutions as those for hollow fiber spinning. Similar to hollow fibers, the flat sheet samples were immersed in tap water for 2 days and subsequently dried in a freeze dryer. The other is the MGO film which were prepared via a pressurized filtration method and then air-dried in ambient conditions³⁷. The procedures to prepare the latter solutions were similar to those in Figure S2 but without the sPPSU polymer. All the samples were kept in a desiccator before FTIR and XPS measurements.

FTIR analyses were carried out with a total of 64 scans over the wavenumber range of 500-4000 cm^{-1} . During the measurements, the sampling chamber was continuously purged with

nitrogen gas at a flow rate of 15 mL/min to avoid signal interference from the surrounding moisture and CO₂. Meanwhile, XPS measurements were performed to analyze the binding energy level of N1s on the membrane surface with a monochromatic X-ray of 15 kV and 100W. The raw spectra were deconvoluted using the XPSPEAK41 software by applying the respective binding energies of N-related structures involved in different chemistry environments.

The shear viscosity of dope solutions was measured by an AR-G2 rheometer (TA Instruments) with a 20-mm cone plate at 25 °C in a shear rate range of 0.1–100 s⁻¹. A power law fluid model was applied to fit the rheological data and to express the relationship between shear stress τ (N/m²) and shear rate $\dot{\gamma}$ (s⁻¹) as follows:

$$\tau = K|\dot{\gamma}|^n \quad (9)$$

Equation (9) is assumed to be applicable to describe the rheological behavior of polymer solutions within the spinnerets during spinning. The shear rate profile of each polymer solution in the spinneret was estimated by the computational fluid dynamics (CFD) model reported by Cao et al.⁴⁴. This CFD model accounts for the flow of a fluid which obeys the power law within a concentric annulus. The shear rate at the outermost of the spinneret outlet was selected to calculate the shear stress since the hollow fibers are outer-selective.

The morphology of the hollow fiber membranes was observed by a field emission scanning electron microscope (FESEM JEOL JSM-6700F). Before observation, the hollow fibers were immersed in liquid nitrogen, fractured, and then coated with platinum using a JEOL JFC-1300 platinum coater. Meanwhile, the surface roughness was observed by atomic force microscopy (AFM, Bruker Dimension ICON) via the tapping mode. The scanning area is kept at 5 × 5 μm.

3. Results and discussion

3.1. Characterizations of the sPPSU hollow fiber membranes

The sPPSU hollow fiber membranes were spun under the conditions described in Table 1. The bore fluid composition and flow rate were varied to optimize the membrane dimension and structural properties which play an important role in separation performance and operational stability. Figure S3 shows the membrane morphology while Figure S4 compares the PWP and PEO rejection of the sPPSU hollow fiber membranes as functions of bore fluid flow rate and chemistry. The PEO rejection shows an up-and-down trend from sPPSU-A1 to sPPSU-A3 with an increase in bore fluid rate. The rejection increases from sPPSU-A1 to sPPSU-A2 is possibly due to a greater bi-axial orientation induced on the outer skin by a higher bore flow rate. However, when the bore flow rate is further increased, additional surface defects may be created, which results in a higher PWP but a lower rejection. The stress-induced orientation and up-and-down trends in rejection have been reported for various membranes⁴⁴⁻⁴⁷. The sPPSU-A2 was selected for GO modifications owing to its decent morphology and better separation characteristics.

3.2. Reaction Scheme

Figure 1 elucidates the possible reaction scheme among MNA, GO and sPPSU. GO is functionalized by MNA via the epoxy-amine nucleophilic addition reaction while the cationic pyridinium ions of MNA probably bind to the sulfonate acid groups of the sPPSU polymer. As a result, MNA serves as the bridge to improve the interfacial interaction between GO and the sPPSU polymer.

Figure 1

The proposed chemical scheme was evidenced by FTIR and XPS results. ATR-FTIR spectra for sPPSU, GO-P, MGO-P and MNA-P flat sheet membranes are shown in Figure S5. It

appears that the peaks at 1323 cm^{-1} (asymmetric stretching) and 1149 cm^{-1} (symmetric stretching) are characteristics of the sulfone group^{48,49}. Other peaks at $600\text{--}720\text{ cm}^{-1}$ (C-S stretching vibration), $800\text{--}900\text{ cm}^{-1}$ (C-H deformation in 1,2,4-substituted phenyl ring), 1107 cm^{-1} (aromatic ring vibration), 1242 cm^{-1} (asymmetric C-O-C stretching of aryl ether group) and 1485 cm^{-1} 1586 cm^{-1} (aromatic C=C stretching) were assigned to the polymer backbone⁴⁸. The sulfonate groups were confirmed by the characteristic peak at 1168 cm^{-1} ^{48, 50, 51}. However, the peaks that features GO and MGO cannot be identified in Figure S5 probably because of their low content in the polymer matrix. In order to confirm the reaction between GO and MNA, neat GO and MGO films were analyzed by FTIR (Transmission mode) and the results are shown in Figure 2. The spectrum of the GO film indicates the presence of hydroxyl groups (OH stretching at 3400 cm^{-1} and C-O stretching at 1055 cm^{-1}) and epoxy groups (C-O-C stretching at 1226 cm^{-1}) as well as carboxyl groups (C=O stretching at 1732 cm^{-1}), which agrees well with the Lerf-Klinowski Model of GO²². MNA powder was also measured for comparison. The MNA spectrum shows a typical broad peak from 3000 to 3400 cm^{-1} , which is the characteristic of the primary amine group. The absence of this peak in the spectra of MGO films indicates that the primary amine groups were converted. Another observation is that the epoxy group at 1226 cm^{-1} vanishes in the spectra of MGO films, indicating that reaction occurred between epoxy groups and amine groups as proposed in Figure 1.

Figure 2

The XPS N1s spectra and their deconvolution results were plotted in Figure 3. The XPS spectra were deconvoluted into three peaks at the binding energies of approximately 401.8 , 400.0 and 399.4 eV , corresponding to the pyridine ring, amide and primary amine groups, respectively. The intensity of the amide group represents the relative amount of MNA that has successfully bound to the GO nanosheets. Interestingly, there are still some unreacted

amine groups for all the three samples even though the films have been thoroughly washed. This may be due to the fact that the amine groups can be hydrogen-bonded with carboxyl and hydroxyl groups. In other words, some unreacted MNA molecules may be trapped in the films via hydrogen-bonding. Thus, the XPS results may indicate an excess of MNA for all the three ratios. The excess of MNA may be due to its relatively low reactivity with GO in NMP solvent.

Figure 3

3.3. Morphology of the nanocomposite membranes

The morphology of the GO- and MGO-incorporated nanocomposite hollow fiber membranes are shown in Figure 4. Compared to the sPPSU-A2 membrane, many small voids can be observed in the cross section of the GO-P membrane. The GO nanosheet image at a high magnification shows an obvious interfacial void with a size more than 1 μm . This is due to the poor interfacial interaction between the GO nanosheets and the polymer matrix.

The interfacial voids are significantly mitigated after the MNA functionalization as shown in Figure 4, indicating that MNA is as an effective bridge between the two parties. In addition, the GO nanosheets can be found on the inner surfaces of both GO-P and MGO-P membranes, as indicated by the red arrows. Interestingly, the numbers of GO nanosheets on the inner surfaces of MGO-P membranes are much higher than that of the GO-P membrane despite of their same initial GO content in the spinning dopes. It is speculated that the GO nanosheets may leach out during phase inversion due to their weak interaction to the polymer matrix. Besides, the cross-sections of the MGO-P membranes exhibit an increasing number of finger-like macrovoids with an increase in MNA content. Since hydrophilic GO has a tendency to hydrogen-bond with water molecules^{37, 52}, the affinity of GO and MGO towards water molecules may induce a faster water intrusion into the membrane. Therefore, the addition of

GO and MGO may accelerate the phase inversion process and facilitate the finger-like structure in the membrane. A similar phenomenon had been reported^{25, 27, 29}.

Figure 4

Another important observation from Figure 4 is that the surface pore size and roughness exhibit distinct differences before and after the MNA modification. AFM imaging results plotted in Figure 5 show that the GO-P membrane has a higher quadratic mean roughness (R_q) than the sPPSU-A2 membrane because of the poor interfacial interaction in the GO-P membrane. A similar phenomenon was reported in literature^{27, 29, 33}. After MNA being introduced, the roughness of the membrane surface is significantly reduced for the MGO-P1 membrane with an R_q value of 6.47 nm. However, R_q increases as a function of MNA content because the excess of unbonded MNA rapidly leaches out during solvent exchange and results in ridges and valleys on the membrane surface. The membrane pore size also becomes larger at higher MNA content. In the case of the MNA-P membrane, it has a larger R_q and surface pore than MGO-P1 even though their original MNA contents are the same. This implies that the rapid release of unbonded MNA into the external coagulant during phase inversion is the main cause to induce a larger surface pore and surface roughness.

Figure 5

3.4. UF performance of the nanocomposite membranes

The PWP and PEO rejection of the GO- and MGO-incorporated nanocomposite membranes and their counterparts were compared in Figure 6. The GO-P membrane exhibits a lower PWP than the sPPSU-A2 membrane even though it has a larger MWCO, suggesting that GO may introduce additional membrane resistance. Interestingly, PWP increases from MGO-P1 to MGO-P3 membranes because of the enlarged surface pore and the MGO-induced finger-like macrovoids as discussed in the previous section. Likewise, the MWCO exhibits a remarkable increase from MGO-P1 to MGO-P3. Especially, compared with the GO-P and

MNA-P membranes, the lowest MWCO of the MGO-P1 membrane confirms our hypothesis that MNA can effectively bridge the GO/polymer interface and eliminate the interfacial voids.

Figure 6

Pore size distributions of all six membranes were plotted in Figure 6. The average pore size follows the sequence of MGO-P1 < sPPSU-A2 < MGO-P2 < MGO-P3 \approx GO-P < MNA-P. In addition to the effect of rapid release of unbonded MNA into the external coagulant during phase inversion, this sequence may be also affected by the incompatibility and the fluid motion of GO in the polymer matrix during spinning. Table 3 tabulates the empirical power law equations for the spinning dopes, and the shear rate and shear stress experienced at the outer surface of the nascent fiber inside the spinneret. The shear rates for all dopes are similar since their spinning conditions are set to be the same. However, due to the difference in shear viscosity, all hollow fibers experience different shear stresses. Interestingly, their shear stresses follow a similar trend to the pore sizes: MGO-sPPSU-1 < sPPSU < MGO-sPPSU-2 < MNA-sPPSU < GO-sPPSU < MGO-sPPSU-3. Since shear viscosity is related to the friction of polymer chains under shear. A low viscosity may indicate that the dope has better chain compatibility with minimal molecular friction under shear. In this regard, the high viscosity of the GO-sPPSU solution may imply poor compatibility between GO and sPPSU. Since GO nanosheets may rotate under shear during spinning, it results in a higher shear stress and a rougher outer surface.

3.5. Fouling study of the nanocomposite membranes in oil-water emulsion

3.5.1. Analysis of fouling mechanism

Figure 7 compares the individual and total membrane resistances as a function of membrane types. Several observations can be made from these results.

Firstly, the membrane hydraulic resistance, R_m , of the GO-P membrane is higher than that of the sPPSU-A2 membrane, which is probably due to additional resistance brought about by the GO nanosheets as aforementioned. After adding MNA to the nanocomposite membranes, an R_m is essentially reduced owing to the increasingly porous structure underneath the selective layer.

Figure 7

Secondly, irreversible fouling-induced resistance, R_{ir} , exhibits a significant decrease from sPPSU-A2 to MGO-P3 while the MNA-P membrane shows a slightly lower value than the sPPSU-A2. R_{ir} is one of the main cursors to evaluate anti-fouling properties of a membrane. It relies on the physiochemical properties of the membrane surface, i.e., pore size, surface roughness and hydrophilicity. A more hydrophilic and less rough surface with proper pores may be preferred to eliminate fouling⁵³. Correlations between surface roughness and R_{ir} are plotted in Figure 8. Interestingly, the R_{ir} values of sPPSU-A2, MNA-P and GO-P membranes are generally negatively correlated to surface roughness, while the R_{ir} values of MGO-P membranes seem not being affected by the surface roughness, except for an insignificant reduction with increasing roughness. These phenomena are probably attributed to the ameliorative hydrophilicity of membrane surfaces brought about by the hydrophilic GO and MNA.

Due to their hydrophilic nature, GO and MGO nanosheets may migrate spontaneously to the membrane/water interface during phase inversion so that the pendant functional groups on GO and MNA would probably dangle towards the water phase in order to lower the interfacial energy³⁰ and thus a hydrophilic surface is attained as indicated in Figure 9. Those hydrophilic pendants may facilitate the formation of a hydration layer on the membrane surface, which prevents irreversible deposition of the foulants. Besides, part of the excess

MNA attached in/on the membrane via ionic interaction may serve the same purpose. Thus, even though a higher roughness and a larger pore size may entice foulant molecules to be lodged in the valleys or pores³³, the nanocomposite membranes shows better anti-irreversible fouling properties at higher MNA content. The slightly lower R_{ir} of the MNA-P membrane may be also ascribed to the ionic bonding with some MNA.

Figure 8

Figure 9

Thirdly, the adsorption-induced resistance, R_{ads} , is found to be negligible in all membranes. This is because adsorption via diffusive mass transfer is a slow process and the accumulation of adsorption fouling during 30 min is minimal even for the pristine sPPSU membrane⁴¹. In contrast, the irreversible fouling-induced resistance, R_r , generally follows the same trend with surface roughness, as illustrated in Figure 8. This implies that R_r may be more sensitive to the surface structure than its hydrophilicity. In other words, in spite of the fact that hydrophilicity may induce easier surface detachment of foulant molecules, surface roughness may take greater effects on R_r in oil-water emulsions. More foulants would be reversibly lodged in the troughs of a rougher surface. The MNA-P membrane exhibits an exceptional R_r , which is probably ascribed to its large surface pores for the foulant accumulation.

As a result, the total resistance, R_t , exhibits a down-and-up trend. Especially, the R_t of MGO-P1 membrane is two-fold and three-fold lower than those of GO-P and MNA-P membranes, respectively. Therefore, the synergistic effects among GO, sPPSU and MNA are the key factors to endow the membrane with proper hydrophilicity and surface morphology for oil-water separation with minimal fouling. Since the R_t increases from MGO-P1 to MGO-P3 membranes, the GO:MNA ratio is another important factor to regulate membrane's physicochemical properties.

3.5.2. Multi-Cycle ultrafiltration tests with periodical backwashing

In order to examine the operational durability and industrial applicability of the nanocomposite hollow fiber membranes for oil-water separation, ultrafiltration experiments were carried out using a laboratory-scale system under cyclic modes, 1 h filtration of oil-water emulsion alternating with 10 min backwashing. The results are summarized in Figure 10.

Figure 10

In order to make a fair comparison, the initial PWP for all six membranes were regulated to similar values at about 260 LMH by adjusting the hydraulic pressure. All fluxes decline prominently within the first few minutes of filtration due to the concentration polarization and kept decreasing slowly until a plateau. All membranes exhibit stable fluxes at the plateau over six cycles with high oil rejections above 95%. Compared to other membranes, the MGO-P1 membrane shows superior anti-fouling properties. Its flux drop is minimal because its more hydrophilic, smoother surface with smaller pores may prevent oil droplets from accumulating on the surface and penetrating into the membrane. Since the flux of MGO-P membranes at the plateau decreases with an increase in MNA content, this may again indicate that excess MNA would deteriorate the anti-fouling properties, which is in good agreement with our previous findings.

4. Conclusions

In this work, different nanocomposite hollow fiber membranes with different fillers, i.e., GO, MGO and MNA, were compared regarding to their microstructures and responses to fouling in an oil-water emulsion. A simultaneously covalent and ionic inter-network was confirmed with the bridging of MNA. Membrane structures were carefully regulated via MNA

modifications with different GO:MNA ratios. An analysis of fouling mechanism unveiled that the MGO-P1 nanocomposite membrane with a GO:MNA ratio of 9:1 showed superior fouling resistances to the others due to its more hydrophilic and smoother surface with a proper pore size. Further increasing the MNA content did not facilitate better anti-fouling properties, instead, a significant increment in reversible fouling was observed because of their higher surface roughness and larger pores. In addition, cyclic UF experiments showed that MGO-P1 exhibited the minimal flux drop amongst all six membranes. The superior anti-fouling properties were achieved due to the contribution of (1) hydrophilicity of GO and MNA (2) appropriate GO:MNA ratio and (3) synergetic effects of GO and MNA to overcome the interfacial voids.

Acknowledgements

The authors would like to thank BASF SE, Germany for funding this work with a grant number of R-279-000-411-597. Thanks are also given to Dr. Y. K. Ong, Ms. L. Luo, Dr. N. Widjojo and Dr. M. Jung for their kind help and suggestions.

Nomenclature

A	Total outer surface area of membrane fibres (m^2)
AFM	Atomic force microscopy
C_f	Concentration of foulant in feed solution (ppm)
C_p	Concentration of foulant in permeate (ppm)
FRR	Flux recovery ratio
FESEM	Field emission scanning electron microscopy
FTIR	Fourier transform infrared spectroscopy
GO	Graphene oxide
J_w	Pure water flux (LMH)

J_{ads}	Pure water flux after adsorption fouling (LMH)
J_{ir}	Pure water flux after irreversible fouling and backwashing (LMH)
K	Power law coefficient constant
M	Permeate mass (kg)
MGO	MNA-functionalized GO
MNA	1-Methylnicotinamide chloride
MWCO	Molecular weight cut-off
NMP	N-Methyl-2-pyrrolidone
n	Power law index
PEG400	Polyethylene glycol, molecular weight 400Da
PEO	Polyethylene oxide
PWP	Pure water permeability (LMH/bar)
R	Rejection
R_a	arithmetic mean roughness (nm)
R_{ads}	Adsorption-induced resistance (m^{-1})
R_{ir}	Irreversible membrane fouling resistance (m^{-1})
R_m	Membrane hydraulic resistance (m^{-1})
R_q	Quadratic mean roughness (nm)
R_r	Reversible membrane fouling resistance (m^{-1})
R_t	Total membrane resistance (m^{-1})
sPPSU	Sulfonated polyphenylsulfone (1.5% sulfonation)
Δt	Permeation time (h)
TMP	Transmembrane pressure (bar)
TOC	Total organic carbon
UF	Ultrafiltration
XPS	X-ray photoelectron spectroscopy
μ	Viscosity of pure water (Pa s)

ρ	Density of permeate (kg/m^3)
τ	Shear stress (N/m^2)
γ	Shear rate γ (s^{-1})

Tables and figures

Table 1. Spinning conditions for sPPSU hollow fiber membranes.

Table 2. Spinning conditions for GO- and MGO-imbedded nanocomposite hollow fiber membranes.

Table 3. Power law equation for spinning solutions and their rheology parameters at outermost of the spinneret.

Figure 1. Reaction Scheme between GO, NMA and sPPSU polymer.

Figure 2. FTIR spectra of GO and MGO films as well as MNA powder.

Figure 3. XPS N1s spectra of the surfaces of (a) MGO-1 (9:1); (b) MGO-2 (4:1) and (c) MGO-3 (2:1) films.

Figure 4. Morphology comparison of the hollow fiber membranes.

Figure 5. AFM images of (a) sPPSU-A2; (b) GO-P; and (c) MGO-P1; (d) MGO-P2; (e) MGO-P3 and (f) MNA-P hollow fiber membranes.

Figure 6. (1) PWP and MWCO and (2) pore size distribution of the hollow fiber membranes.

Figure 7. Membrane resistances of hollow fiber membranes based on the resistance-in-series model.

Figure 8. Correlations between surface roughness and irreversible/reversible fouling-induced resistances.

Figure 9. Illustration of the role of GO in the nanocomposite membrane for fouling control.

Figure 10. Time-dependent flux of different membranes with intermittent backwashing in oil-water emulsion.

Figure S1. Molecular structure of 1.5sPPSU, where p:q = 98.5:1.5.

Figure S2. Preparation of MGO-sPPSU dope solutions.

Figure S3. Morphology of the sPPSU hollow fiber membranes.

Figure S4. PWP and PEO rejection of the sPPSU hollow fiber membranes.

Figure S5. FTIR spectra of sPPSU, GO-sPPSU, MGO-sPPSU and MNA-sPPSU flat-sheet membranes.

References

1. A. Cassano and A. Basile, in *Advanced Membrane Science and Technology for Sustainable Energy and Environmental Applications*, Woodhead Publishing Limited, 2011, pp. 647-679.
2. Y. Zhu, D. Wang, L. Jiang and J. Jin, *NPG Asia Mater.*, 2014, 6, e101.
3. M. Padaki, R. Surya Murali, M. S. Abdullah, N. Misdan, A. Moslehyani, M. A. Kassim, N. Hilal and A. F. Ismail, *Desalination*, 2015, 357, 197-207.
4. M. Cheryan and R. N., *J. Membr. Sci.*, 1998, 151, 13-28.
5. F.-R. Ahmadun, A. Pendashteh, L. C. Abdullah, D. R. Biak, S. S. Madaeni and Z. Z. Abidin, *J. Hazard. Mater.*, 2009, 170, 530-551.
6. J. Kim and B. Van der Bruggen, *Environ. Pollut.*, 2010, 158, 2335-2349.
7. J. L. Nilsson, *J. Membr. Sci.*, 1990, 52, 121-142.
8. S. S. Sablani, M. F. A. Goosen, R. Al-Belushi and M. Wilf, *Desalination*, 2001, 141, 269-289.
9. W. Gao, H. Liang, J. Ma, M. Han, Z.-l. Chen, Z.-s. Han and G.-b. Li, *Desalination*, 2011, 272, 1-8.
10. Y. J. Shih and Y. Chang, *Langmuir*, 2010, 26, 17286-17294.
11. J. Peng, Y. Su, Q. Shi, W. Chen and Z. Jiang, *Bioresour. Technol.*, 2011, 102, 2289-2295.
12. Q.-F. An, W.-D. Sun, Q. Zhao, Y.-L. Ji and C.-J. Gao, *J. Membr. Sci.*, 2013, 431, 171-179.
13. J. R. Du, S. Peldszus, P. M. Huck and X. Feng, *J. Membr. Sci.*, 2015, 475, 488-495.
14. Y. Chang, C.-Y. Ko, Y.-J. Shih, D. Quémener, A. Deratani, T.-C. Wei, D.-M. Wang and J.-Y. Lai, *J. Membr. Sci.*, 2009, 345, 160-169.
15. T.-H. Bae and T.-M. Tak, *J. Membr. Sci.*, 2005, 249, 1-8.
16. Y. Yang, P. Wang and Q. Zheng, *J. Polym. Sci., Part B: Polym. Phys.*, 2006, 44, 879-887.

17. L. Shao, Z. X. Wang, Y. L. Zhang, Z. X. Jiang and Y. Y. Liu, *J. Membr. Sci.*, 2014, 461, 10-21.
18. L. Yan, Y. S. Li and C. B. Xiang, *Polymer*, 2005, 46, 7701-7706.
19. Z. Wang, H. Yu, J. Xia, F. Zhang, F. Li, Y. Xia and Y. Li, *Desalination*, 2012, 299, 50-54.
20. F. Jin, W. Lv, C. Zhang, Z. Li, R. Su, W. Qi, Q.-H. Yang and Z. He, *RSC Adv.*, 2013, 3, 21394-21397.
21. L. Shao, X. Cheng, Z. Wang, J. Ma and Z. Guo, *J. Membr. Sci.*, 2014, 452, 82-89.
22. D. R. Dreyer, S. Park, C. W. Bielawski and R. S. Ruoff, *Chem. Soc. Rev.*, 2010, 39, 228-240.
23. B. Mi, *Science*, 2014, 343, 740-742.
24. K. Huang, G. Liu, Y. Lou, Z. Dong, J. Shen and W. Jin, *Angew. Chem. Int. Ed.*, 2014, 53, 6929-6932.
25. C. Zhao, X. Xu, J. Chen and F. Yang, *J. Environ. Chem. Eng.*, 2013, 1, 349-354.
26. J. Lee, H.-R. Chae, Y. J. Won, K. Lee, C.-H. Lee, H. H. Lee, I.-C. Kim and J.-m. Lee, *J. Membr. Sci.*, 2013, 448, 223-230.
27. L. Yang, B. Tang and P. Wu, *J. Mater. Chem. A*, 2014, 2, 18562-18573.
28. L. Yu, Y. Zhang, B. Zhang, J. Liu, H. Zhang and C. Song, *J. Membr. Sci.*, 2013, 447, 452-462.
29. Z. Xu, J. Zhang, M. Shan, Y. Li, B. Li, J. Niu, B. Zhou and X. Qian, *J. Membr. Sci.*, 2014, 458, 1-13.
30. H. Zhao, L. Wu, Z. Zhou, L. Zhang and H. Chen, *Phys. Chem. Chem. Phys.*, 2013, 15, 9084-9092.
31. C. A. Crock, A. R. Rogensues, W. Shan and V. V. Tarabara, *Water Res.*, 2013, 47, 3984-3996.

32. M. Safarpour, A. Khataee and V. Vatanpour, *Ind. Eng. Chem. Res.*, 2014, 53, 13370-13382.
33. J. Zhang, Z. Xu, W. Mai, C. Min, B. Zhou, M. Shan, Y. Li, C. Yang, Z. Wang and X. Qian, *J. Mater. Chem. A*, 2013, 1, 3101-3111.
34. J. Zhang, Z. Xu, M. Shan, B. Zhou, Y. Li, B. Li, J. Niu and X. Qian, *J. Membr. Sci.*, 2013, 448, 81-92.
35. L. Y. Ng, A. W. Mohammad, C. P. Leo and N. Hilal, *Desalination*, 2013, 308, 15-33.
36. Y. P. Tang, N. Widjojo, G. M. Shi, T. S. Chung, M. Weber and C. Maletzko, *J. Membr. Sci.*, 2012, 415-416, 686-695.
37. Y. P. Tang, D. R. Paul and T. S. Chung, *J. Membr. Sci.*, 2014, 458, 199-208.
38. W.-S. Hung, C.-H. Tsou, M. De Guzman, Q.-F. An, Y.-L. Liu, Y.-M. Zhang, C.-C. Hu, K.-R. Lee and J.-Y. Lai, *Chem. Mater.*, 2014, 26, 2983-2990.
39. J. J. Qin and T. S. Chung, *J. Membr. Sci.*, 1999, 157, 35-51.
40. K. Y. Wang, T. Matsuura, T. S. Chung and W. F. Guo, *J. Membr. Sci.*, 2004, 240, 67-79.
41. L. Luo, G. Han, T. S. Chung, M. Weber, C. Staudt and C. Maletzko, *J. Membr. Sci.*, 2015, 476, 162-170.
42. P. Li, S. S. Lim, J. G. Neo, R. C. Ong, M. Weber, C. Staudt, N. Widjojo, C. Maletzko and T. S. Chung, *Ind. Eng. Chem. Res.*, 2014, 53, 14056-14064.
43. P. Rai, C. Rai, G. C. Majumdar, S. DasGupta and S. De, *J. Membr. Sci.*, 2006, 283, 116-122.
44. C. Cao, T. S. Chung, S. B. Chen and Z. Dong, *Chem. Eng. Sci.*, 2004, 59, 1053-1062.
45. J. J. Qin, R. Wang and T. S. Chung, *J. Membr. Sci.*, 2000, 175, 197-213.
46. N. Peng and T. S. Chung, *J. Membr. Sci.*, 2008, 310, 455-465.
47. Y. Wang, M. Gruender and T. S. Chung, *J. Membr. Sci.*, 2010, 363, 149-159.

48. B. C. Johnson, İ. Yilgör, C. Tran, M. Iqbal, J. P. Wightman, D. R. Lloyd and J. E. McGrath, *J. Polym. Sci., Polym. Chem. Ed.*, 1984, 22, 721-737.
49. S. Arnold and R. A. Assink, *J. Membr. Sci.*, 1988, 38, 71-83.
50. Y. Matsumoto, M. Sudoh and Y. Suzuki, *J. Membr. Sci.*, 1999, 158, 55-62.
51. G. Socrates, *Infrared and Raman Characteristic Group Frequencies*, John Wiley & Sons. LTD, England, 2001.
52. T.-M. Yeh, Z. Wang, D. Mahajan, B. S. Hsiao and B. Chu, *J. Mater. Chem. A*, 2013, 1, 12998-13003.
53. D. Rana and T. Matsuura, *Chem. Rev.*, 2010, 110, 2448-2471.

Table 1. Spinning conditions for sPPSU hollow fiber membranes.

Spinning parameter	Conditions				
Dope composition (wt%)	12/25/58/5 (sPPSU/PEG400/NMP/H ₂ O)				
Bore fluid composition (wt%)	90/10 (NMP/water)			80/20(NMP/water)	
Bore flow rate (mL/min)	3	5	7	5	7
Membrane code	sPPSU-A1	sPPSU-A2	sPPSU-A3	sPPSU-B2	sPPSU-B3
Membrane OD (μm)	980	1040	1090	1300	1410
Wall thickness (μm)	200	180	170	210	200

Table 2. Spinning conditions for GO- and MGO-imbedded nanocomposite hollow fiber membranes.

Spinning parameter	Conditions				
Dope composition (wt%)	12/25/58/5 (Solid/PEG400/NMP/H ₂ O)				
Bore fluid composition (wt%)	90/10(NMP/water)				
GO concentration in polymer (wt%)	0.57				
GO/MNA ratio	1:0	9:1	4:1	2:1	0:1
Bore flow rate (mL/min)	5				
Membrane code	GO-P	MGO-P1	MGO-P2	MGO-P3	MNA-P
Membrane OD (μm)	1050	1080	1100	1100	1080
Wall thickness (μm)	210	190	200	200	190

Table 3. Power law equation for spinning solutions and their rheology parameters at outermost of the spinneret.

		sPPSU	GO-sPPSU	MGO-sPPSU-1	MGO-sPPSU-2	MGO-sPPSU-3	MNA
$\tau = K \dot{\gamma} ^n$	K	15.08	10.20	17.44	11.59	10.49	13.61
	n	0.5964	0.7303	0.5535	0.6532	0.7554	0.6718
Shear rate $\dot{\gamma}$ (s ⁻¹)		1556	1440	1605	1502	1423	1485
Shear stress τ (N/m ²)		1208	2127	1037	1368	2528	1840

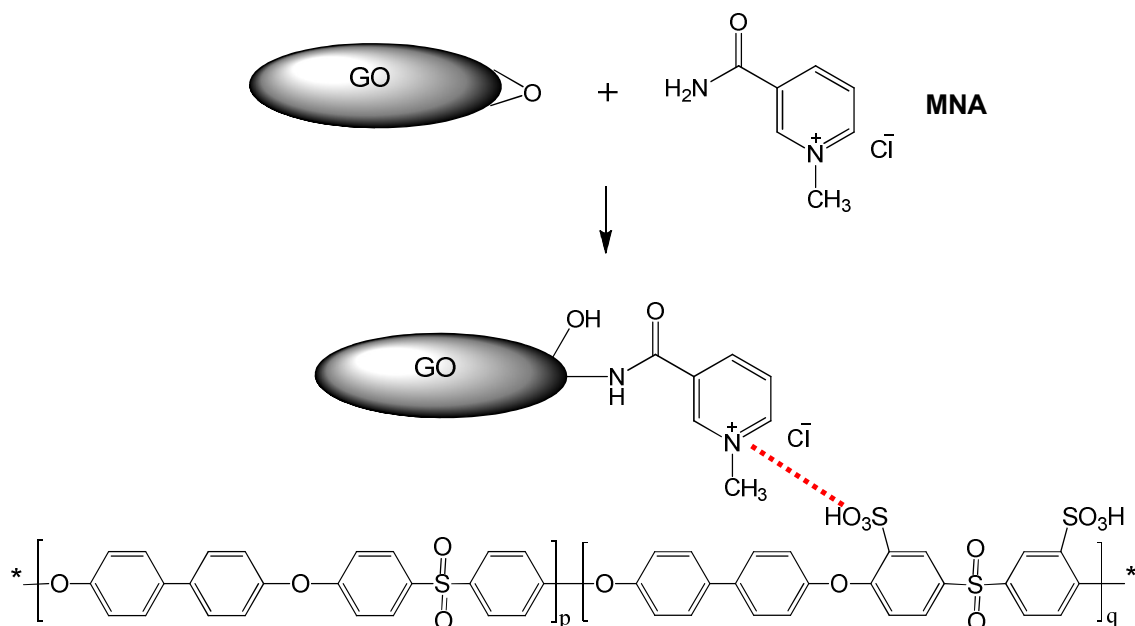


Figure 1. Reaction Scheme between GO, MNA and sPPSU polymer.

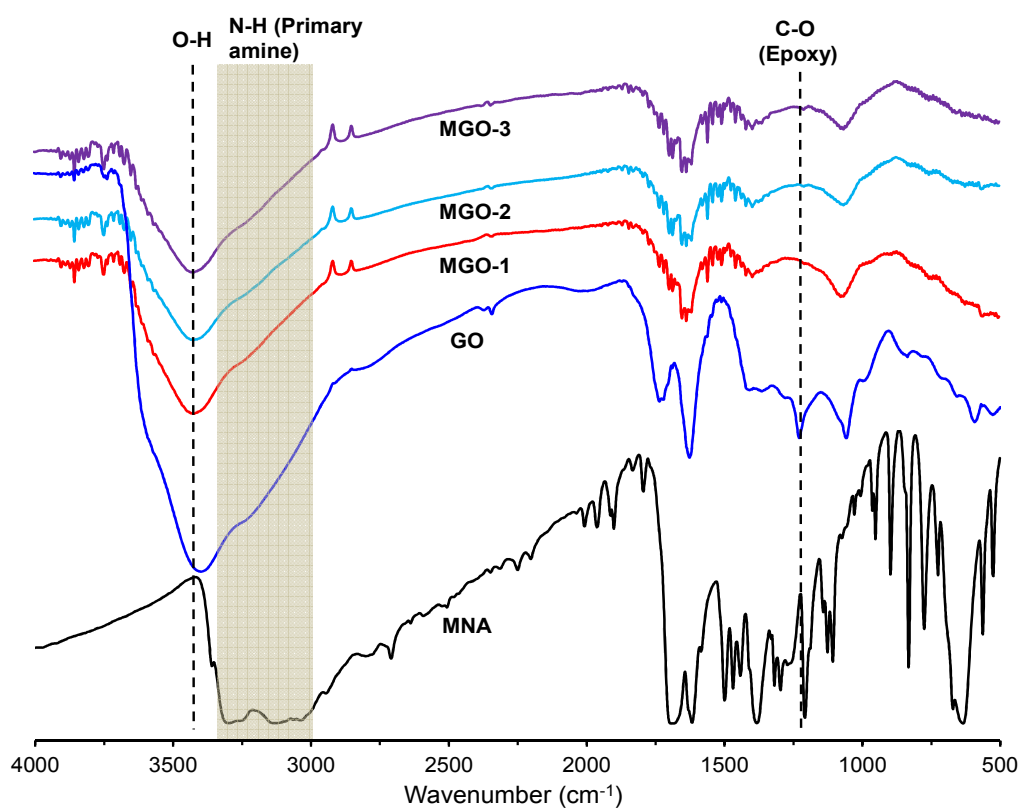


Figure 2. FTIR spectra of GO and MGO films as well as MNA powder.

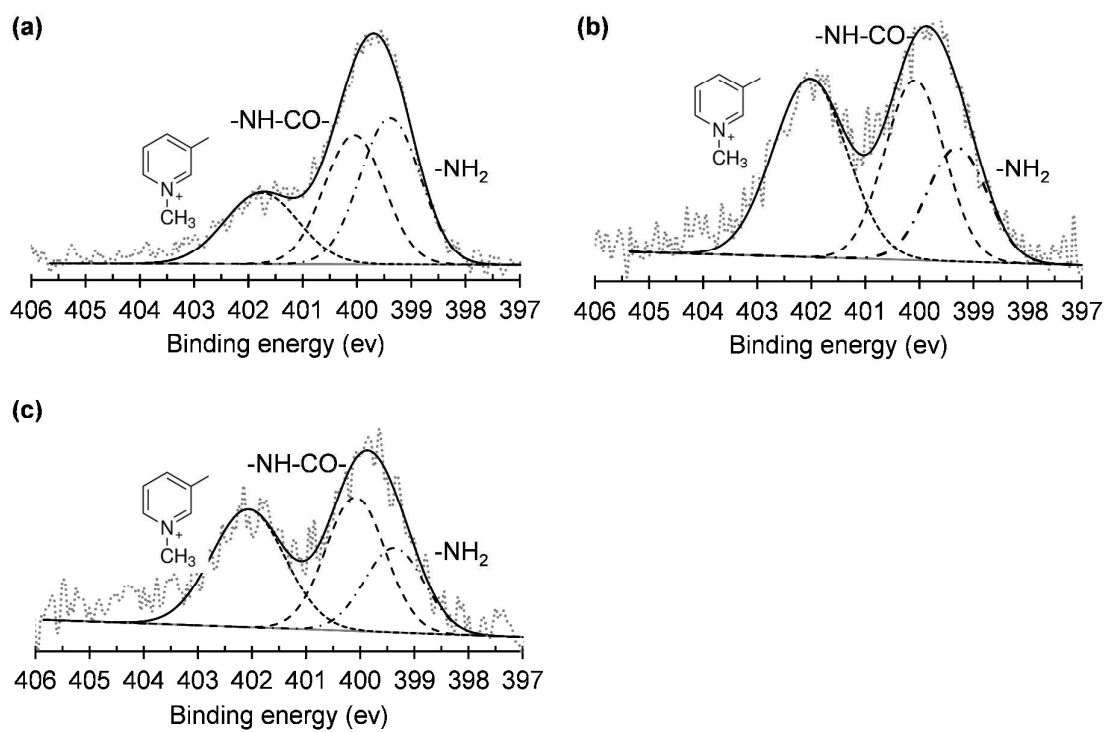


Figure 3. XPS N1s spectra of the surfaces of (a) MGO-1 (9:1); (b) MGO-2 (4:1) and (c) MGO-3 (2:1) films.

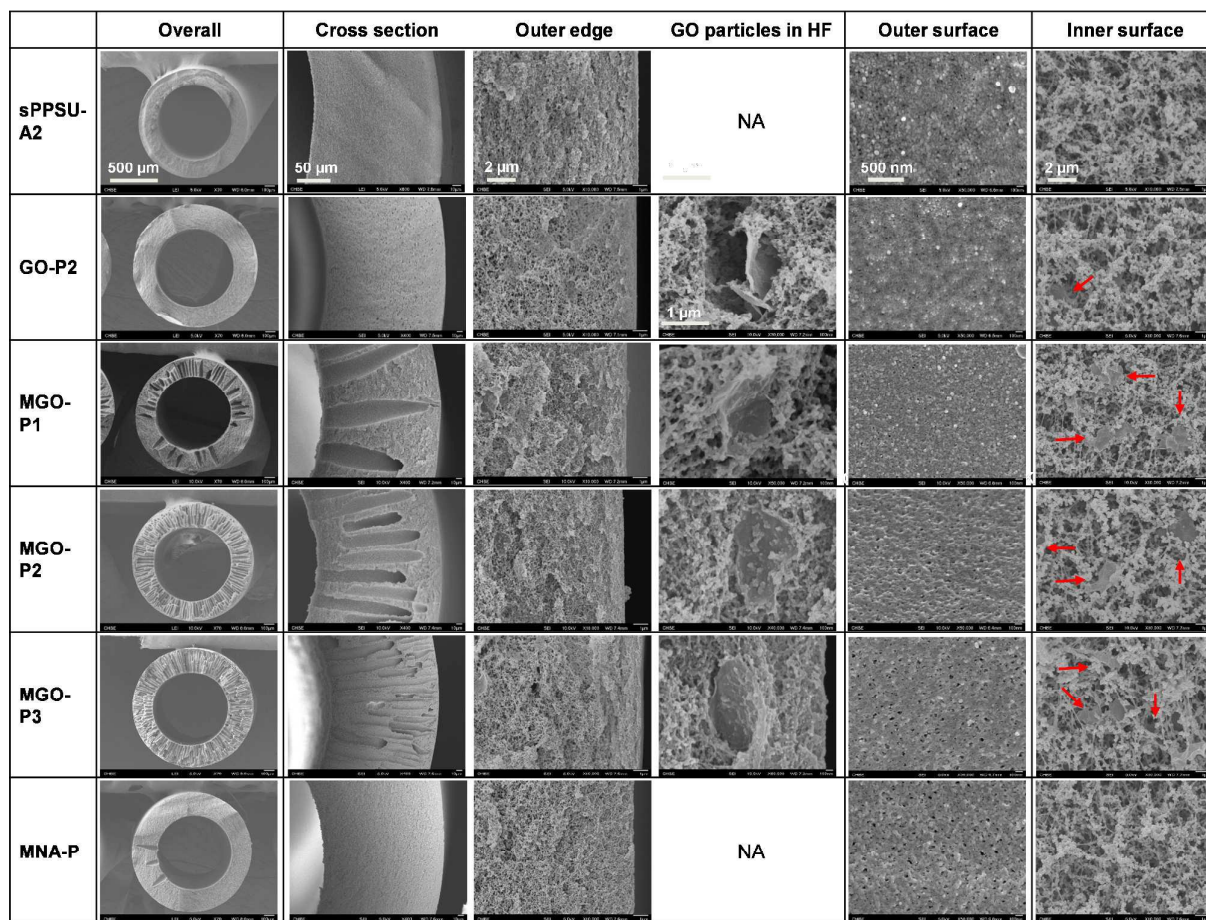


Figure 4. Morphology comparison of the hollow fiber membranes.

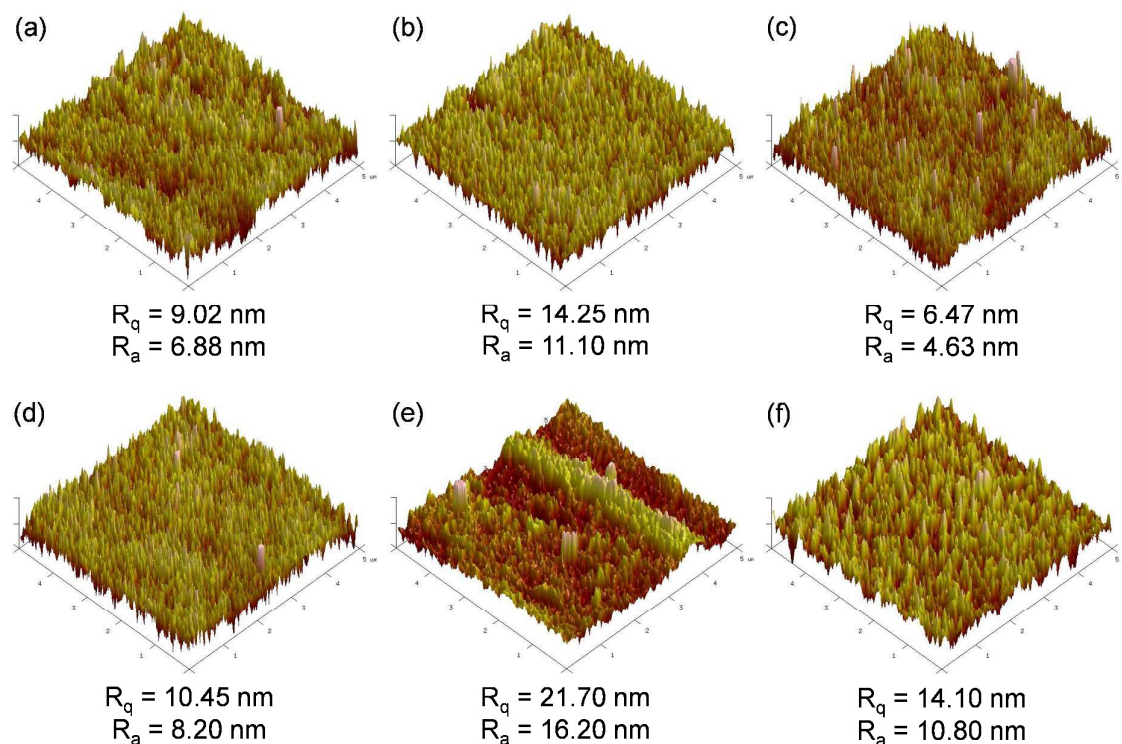


Figure 5. AFM images of (a) sPPSU-A2; (b) GO-P; and (c) MGO-P1; (d) MGO-P2; (e) MGO-P3 and (f) MNA-P hollow fiber membranes.

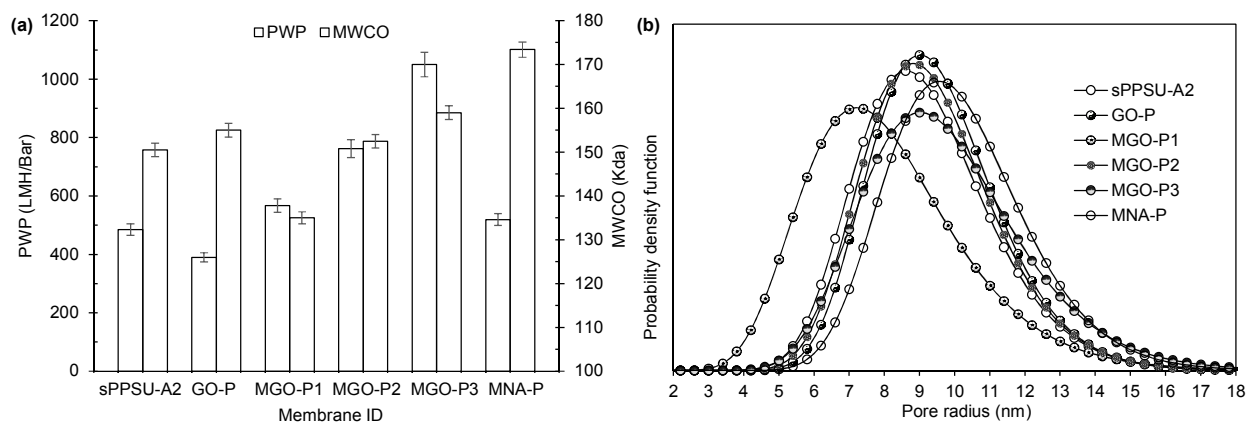


Figure 6. (1) PWP and MWCO and (2) pore size distribution of the hollow fiber membranes.

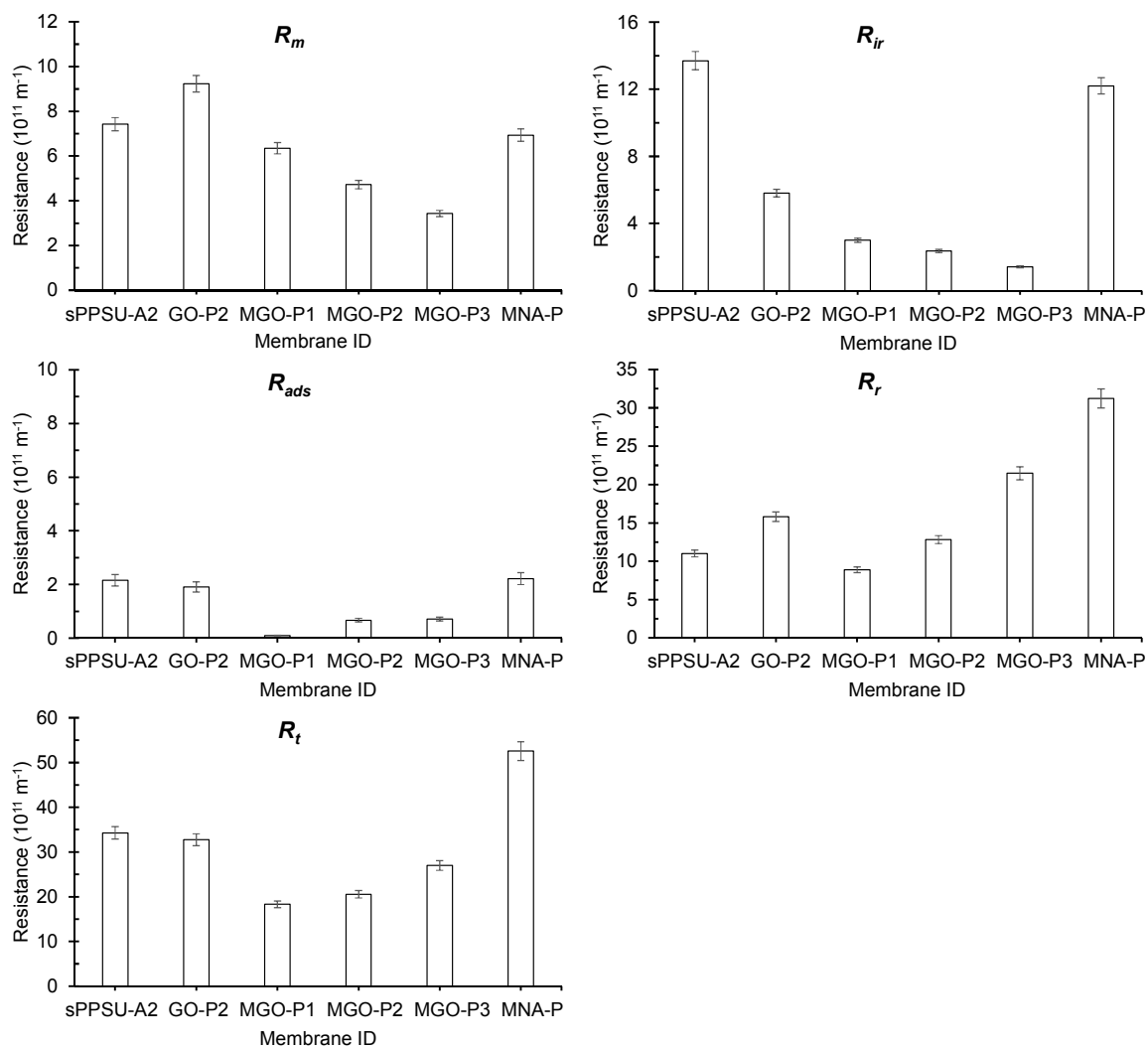


Figure 7. Membrane resistances of hollow fiber membranes based on the resistance-in-series model.

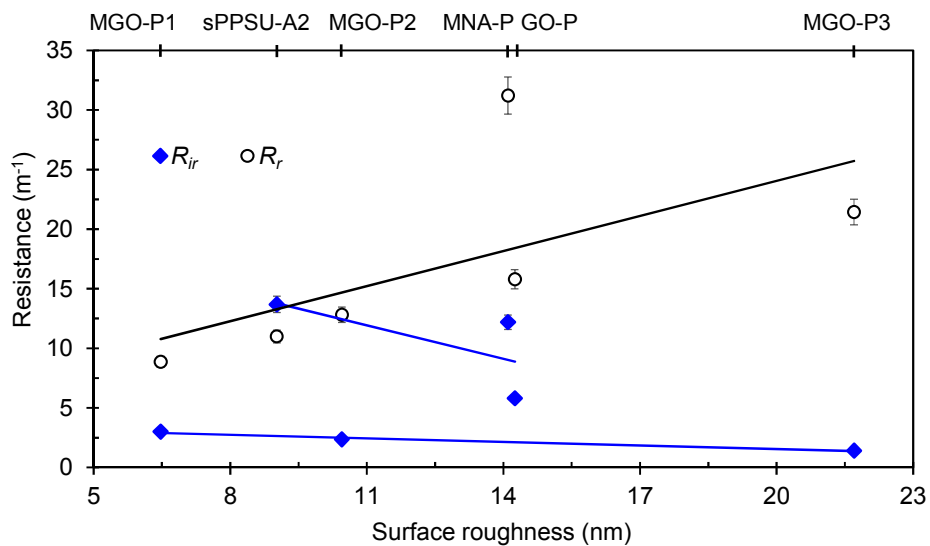


Figure 8. Correlations between surface roughness and irreversible/reversible fouling-induced resistances.

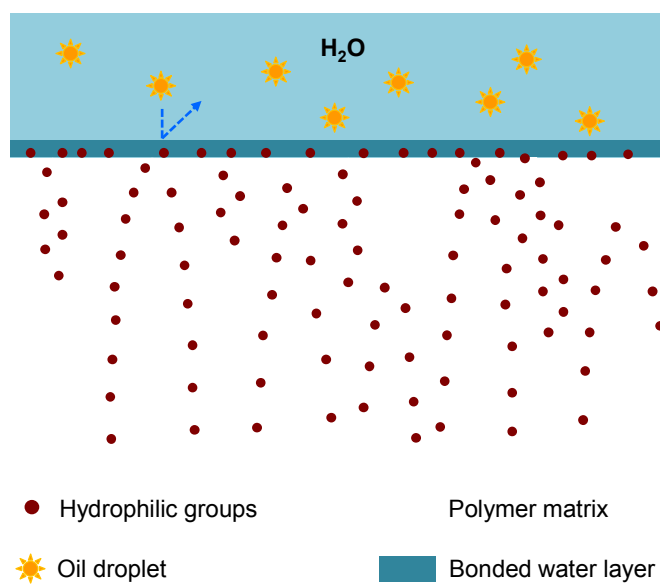


Figure 9. Illustration of the role of GO in the nanocomposite membrane for fouling control.

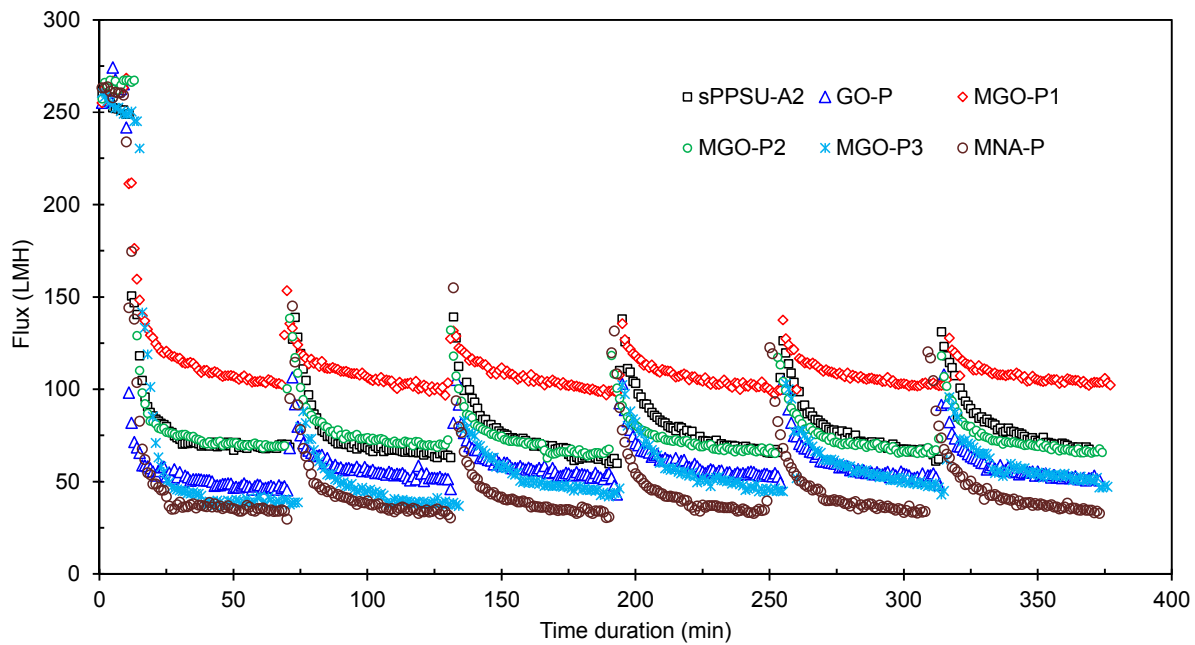


Figure 10. Time-dependent flux of different membranes with intermittent backwashing in oil-water emulsion.